Dynamic Control of Formula - Towards Driverless

Jing Lu

A thesis

submitted in partial fulfillment of the
requirements for the degree of

Master of Science in Mechanical Engineering

University of Washington
2020

Committee:
Ashley F. Emery
Robert B. Darling
Joseph Garbini

Program Authorized to Offer Degree:
Mechanical Engineering

Abstract

Dynamic Control of Formula - Towards Driverless

Jing Lu

Chair of the Supervisory Committee:

Ashley F. Emery

Department of Mechanical Engineering

This paper presents vehicle dynamic control algorithms for a dual-motor rear-wheel-drive electric racing car of UW Formula Motorsports. Team-31 vehicle was designed for human driver only, so the team proposed an PID (proportional-integral-derivative) based yaw rate and slip ratio control on dynamic bicycle or four-wheel vehicle dynamics model. The algorithm aimed to improve acceleration behavior in straight-line event and cornering maneuverability. It will also serve as the low-level stability control for the future autonomous racing car.

Team-32 aimed to compete in FSG driverless events in 2022 - 2023, so the control system should merge into autonomous driving hardware platform with a MPC (model predictive control) based trajectory tracking algorithm. Vehicle behavior and control effectiveness were analyzed using MATLAB Simulink, and hopefully would be validated in HiL (Hardware-in-loop) setup or RC car in the future.

In Section 2: Vehicle handling and performance, the author explained the derivation of vehicle lateral and longitudinal dynamics model, critical parameters for cornering behavior evaluation and their effects on turn stability. Analysis of a traditional torque vectoring and traction control strategy was explained under steady states condition. In section 3: Model predictive control for autonomous driving, an optimization-based trajectory tracking method was introduced based on kinematic vehicle model. The controller behavior was evaluated under simulated competition events. Section 4: Hardware implementation covered key points in modeling and configuring critical actuators and sensors for vehicle test preparation.

Contents

1 Introduction

1.1 Dynamic Control Milestones

Vehicle dynamic control (torque vectoring and traction control) was a widely applicable technology on commercial, racing, and off-road vehicles. One of its earliest applications was a direct yaw moment control with brakes, proposed by Mitsubishi engineers in 1996. The algorithm regulates yaw moment on vehicle regardless of its acceleration or braking, to improve cornering maneuvers of a rally car. Since then, various torque vectoring system have been implemented to improve vehicle dynamics on AWD and RWD vehicle (Kaoru and Yuichi 2008). Ricardo Company officially introduced the term "torque vectoring" in SAE 2006-01-08, to describe a novel rear axle design that achieve bi-directional torque control with epicyclic gear arrangement (Wheals, Deane, Drury and Griffith 2006).

Figure 1: Mitsubishi Evo & S-AWC Yaw Control System

Due to a rising demand on electric vehicle, recent studies focused on torque distribution among motors based on classical or modern control theories. Balasharmila and Joerg (2014) proposed a Proportional-Integral-Derivative (PID) feedback control of rear motor torque difference based on steering angle and motor speeds, but the vehicle dynamics model contained too many parameters that were hard to measure and estimate in real time, such as cornering radius and slip angle. Goran and Stjepan (2016) proposed an MPC algorithm based on quadratic programming optimization. The system enhanced vehicle maneuverability in critical conditions, such as ice driving in simulation. But solving optimization in each sampling period required excessive computational power in the implementation. Leonarde, Aldo, Patrick, and Andrew (2014) compared sliding-mode controller with conventional and adaptive PID control. The results showed sliding-mode controller, although provided additional robustness, would cause undesirable oscillation in yaw rate during high amplitude step steer. Adaptive PID with gain scheduling would not necessarily compensate for vehicle yaw rate response at various operating points.

Due to limited computational resources, ease of implementation, predictable time and frequency domain response proven by literatures, the author adopted a nested PID control based on yaw rate and slip ratio. The yaw rate measured by IMU would continuously track the ideal cornering behavior, while the slip angle and slip ratio estimated longitudinal and lateral frictional coefficient to calculate real-time tractions and side forces.

1.2 Autonomous Driving Overview

In the past few decades, autonomous driving technology thrived both in the automotive industry and academia. In 2004, the United States Government funded the first DARPA Grand Challenge, aiming to explore the potential of unmanned ground vehicle navigating through miles of terrain with natural obstacles. James Albus from the National Institute of Standards and Technology proposed a hierarchical control based Real-Time Control System. The competition was held again in 2005 within harsh desert environments. David Hall of Velodyne competed with a prototype LiDAR, which later became a popular industry-level integrated sensor for

mainstream manufactures. 2007 marked the third DARPA events, during which the CMU autonomous Chevy Tahoe won the first place in urban environment racing with a model-based trajectory generation algorithm for path planning.

Figure 2: CMU vehicle in DARPA Challenge

The SAE association evaluated current autonomous driving system from 0 to 5:

- Level 0: No Driving Automation. Driving tasks are under fully manual control of human.
- Level 1: Driver Assistance: The vehicle features a single throttling or steering control given information about driving environment (cruise control / lane keeping), while the human driver performed all remaining tasks.
- Level 2: Partial Automation: Commonly named ADAS (advanced driver-assistance system). The vehicle features both throttling and steering control given information (distance to the front vehicle, road lines). Many vehicles in the market nowadays (Tesla, Ford, GM) are qualified at this level.
- Level 3: Conditional Automation: The vehicle is capable of full driving tasks but may request human intervention in certain scenarios. Vehicle should assume human decision to be appropriate.
- Level 4: High Automation: The vehicle is capable of decision-making under most driving environments and intervene system failure. Human may still override, but the decision will not be assumed appropriate.
- Level 5: Full Automation: The vehicle handles the full driving task.

1.3 FSG Motivation

The Formula Student Germany (FSG) driverless competition requires team to build a level 2 autonomous vehicle, which performs straight line acceleration, skid-pad (a figure-8), autocross, track drive and emergency braking tests. The vehicle hardware system contains the following module in series: perception, trajectory planning, control, and low-level actuation units.

Figure 3: Cone Detection and SLAM in FSG

The perception module, containing stereo camera (with an optional LiDAR) will recognize blue and yellow traffic cones as the track boundary. Tensorflow and Nvidia Jetson Xavier machine is an ideal tool chain for

computer vision. After receiving data from perception module, a FastSLAM algorithm will generates way points as reference trajectory for the future time steps. The MPC controller shall conduct a local optimization based on generated waypoints to perform a centerline following or optimal trajectory driving. Upon tracking the trajectory with a nonlinear optimization method, a traditional torque vectoring and traction control will be used for stability control.

2 Vehicle Handling Performance

There are two major topics in the vehicle dynamics study: Analysis of vehicle handling and stability with the body-tire force model, and analysis of riding comfort with spring-mass-damper model. The riding comfort perspectives are determined by suspension geometries and characteristics. Handling and stability analysis on the other hand, focus more on longitudinal and lateral dynamics properties, which will be stressed in this section. The term handling referees to the lateral (cornering) behavior of the vehicle. Its performance objectives can be generally concluded as:

- Responsiveness of vehicle to driver's steering input.
- Ease of control under external disturbance.
- Intuitive recognition of handling limits.
- Impacts of changing parameters (passenger loads, tire road surface) should be minimized.

Traditionally, the handling shall be measured with a "closed-loop" performance of vehicle-driver combination shown in Figure 4. It is rather pointless to analyze system as such in normal driving scenarios since the driver behavior as controller is unique. Hence, most studies focus on dynamic itself as an "open-loop" performance. However, it is still meaningful to model the driver responsive time as time delay of controller when discussing critical situations, such as stability under high speed driving.

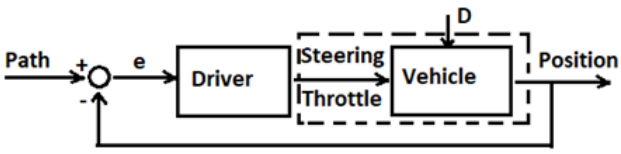

Figure 4: Vehicle Driver "Closed-Loop" System

Traditionally, the handling shall be measured with a "closed-loop" performance of vehicle-driver combination shown in Figure 4. It is rather pointless to analyze system as such in normal driving scenarios since the driver behavior as controller is unique. Hence, most studies focus on dynamic itself as an "open-loop" performance. However, it is still meaningful to model the driver responsive time as time delay of controller when discussing critical situations, such as stability under high speed driving.

2.1 Bicycle Model

For primitive analysis of handling characteristic, the body dynamics will be simplified as a single-track bicycle. Assuming a vehicle with high stiffness suspension riding on the flat ground, it is reasonable to ignore vertical motion, suspension dynamic, left-right weight transfer and aerodynamics. Front-rear weight transfer can be ignored at low speed.

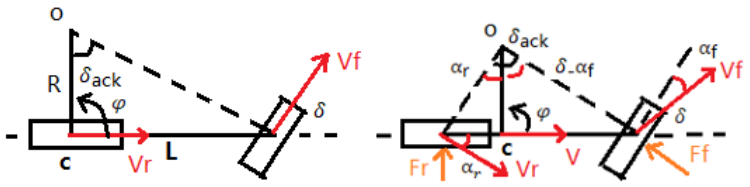

Figure 5: Kinematic and Dynamic Bicycle Model

Taking an example of dynamic bicycle model with linear tire, only lateral tire forces are generated. The motion is constrained to X-Y plane only, with longitudinal speed V as constant. The vehicle behaves as a rigid body for lateral and yaw motion. Under small δ angle approximation: $\sin\delta = \delta, \cos\delta = 1, \tan\delta = \delta$.

Reference point C is the vehicle CG. Denoting m = vehicle mass, I_z as moment of inertia about Z-axis, a and b be the distance from C to front and rear axle (wheelbase). C_f and C_r be the cornering stiffness. Equations of motion can be formulated based on tire model, forces, and momentum equilibrium around CG. Using lateral velocity and yaw rate as control variable. Linearized system dynamics for can be described as:

$$v_y' = -(\frac{C_f + C_r}{mv_x}) + (\frac{bC_r - aC_f}{mv_x} - v_x)\phi' + (\frac{C_f}{m})\delta \tag{1}$$

$$\ddot{\phi} = (\frac{bC_r - aC_f}{I_z v_x} - v_x)v_y - (\frac{a^2C_f - b^2C_r}{I_x v_x})\phi' + (\frac{aC_f}{I_z})\delta \tag{2}$$

An equivalent state-space model using steering angle as input:

$$\begin{gathered} \dot{x} = Ax + Bu \\ x = \begin{bmatrix} v_y \\ \dot{\phi} \end{bmatrix}; \dot{x} = \begin{bmatrix} \dot{v_y} \\ \ddot{\phi} \end{bmatrix}; u = \delta \\ \frac{d}{dt}\begin{bmatrix} v_y \\ \dot{\phi} \end{bmatrix} = \begin{bmatrix} -(\frac{C_f+C_r}{mv_x}) & (\frac{bC_r-aC_f}{mv_x} - v_x) \\ (\frac{bC_r-aC_f}{I_z v_x} - v_x) & -(\frac{a^2C_f-b^2C_r}{I_z v_x}) \end{bmatrix}\begin{bmatrix} v_y \\ \dot{\phi} \end{bmatrix} + \begin{bmatrix} \frac{C_f}{m} \\ \frac{aC_f}{I_z} \end{bmatrix}\delta \\ C = \begin{bmatrix} 1 & 0 \\ 0 & 1 \end{bmatrix}; D = \begin{bmatrix} 0 \end{bmatrix}; \end{gathered} \tag{3}$$

For torque vectoring, an additional yaw moment $\begin{bmatrix} 0 \\ \frac{1}{I_z} \end{bmatrix} M_z$ or torque difference $\begin{bmatrix} 0 \\ \frac{1}{0.05I_z} \end{bmatrix} \Delta T$ will be added to Bu.

2.2 Yaw Stability

To achieve yaw stability with linear bicycle model, eigenvalues of the system should be on left hand plane (LHP). Finding determinant of A as:

$$\begin{gathered} det(SI - A) = 0 \\ (S + \frac{C_f + C_r}{mv_x})(S + \frac{a^2C_f + b^2C_r}{I_z v_x})(v_x - \frac{bC_r - aC_f}{mv_x})(\frac{+b^2C_r - a^2C_f}{I_z v_x}) = 0 \end{gathered} \tag{4}$$

Rearranging the formula into:

$$S^2 + BS + C = 0 \rightarrow S_{1,2} = \frac{1}{2}(-B \pm \sqrt{B^2 - 4C}) \tag{5}$$

with

$$B = \frac{I_z(C_f + C_r) + m(a^2C_f + b^2C_r)}{mI_z v_x}, \; C = \frac{mv_x^2(b^2C_r) - a^2C_f) + C_f C_r(a+b)^2}{mI_z v_x} \tag{6}$$

B is consisted of suspension parameters, mass, and inertia which are always positive. The following cases are considered:
(1).$B^2 - 4C < 0 \rightarrow S_{1,2} = -\frac{1}{2}B \pm j\omega, \omega = \sqrt{4C - B^2}$
(2).$B^2 > B^2 - 4C \geq 0 \rightarrow S_{1,2} = \frac{1}{2}(-B \pm \sqrt{B^2 - 4C})$
(3).$C \leq 0, B - 4C^2 \geq B^2 \rightarrow S_{1,2} = \frac{1}{2}(-B \pm \sqrt{B^2 - 4C})$

For case (1) and (2), all eigenvalues have negative real parts, system stable. While in case (3) system is unstable due to one positive real part.In conclusion, $C > 0$ is the necessary and sufficient condition for vehicle yaw stability. Following observations can be made from the expression of C:

(1).Since vehicle parameters are always positive, the value of C is dominant by the term $C_f C_r (a + b)^2$ on numerator for sufficiently small v_x. At low speed a positive C always hold, and vehicle should be stable.
(2).For $b^2 C_r - a^2 C_f > 0$, a positive term is added under all v_x. Hence the vehocle with longer wheelbase and higher cornering stiffness tends to be stable.
(3).If $b^2 C_r - a^2 C_f < 0$, the vehicle tends to be unstable when v_x exceeds a critical speed so that $C \leq 0$.

2.3 Understeer & Oversteer

With the bicycle model, one of the most important parameters for handling performance evaluation: understeer gradient can be derived. Let O be the instantaneous center of rotation of a bicycle model. C be the point of kinematic bicycle model where the slip angle $\alpha = 0$. The tangential radius R is defined as length between OC. The Ackermann steer angle δ_{ack} is defined as the angle between the line from O to the midpoint of the rear wheel and front wheel. On kinematic model, direction local velocity vectors v_f and v_r equals to vehicle orientation. the following relationship can be derived:

$$\begin{aligned} \delta_{ack,kin} &= \delta_{kin} \\ tan(\delta_{ack}) = tan(\delta_{kin}) &= \frac{L}{R} \\ \delta_{kin} &= atan(\frac{L}{R}) \end{aligned} \tag{7}$$

Velocity vectors on dynamic model deviate from wheel orientations due to existence of the slip angle α. Based on geometry:

$$\begin{aligned} tan(\alpha_r) = \frac{b}{R}, tan(\delta - \alpha_r) &= \frac{a}{R} \\ \delta_{ack.dyn} = \delta_{dyn} - \alpha_f + \alpha_r &= atan(\frac{a}{r}) + atan(\frac{b}{R}) \end{aligned} \tag{8}$$

Under small angle approximation, Ackermann steering angle of kinematic and dynamic model can be written as:

$$\delta_{ack,kin} = atan(\frac{L}{R}) \approx \frac{L}{R} \tag{9}$$

$$\delta_{ack,dyn} = atan(\frac{a}{R}) + atan(\frac{b}{R}) \approx \frac{a}{R} + \frac{b}{R} \tag{10}$$

The most basic experiment to assess open-loop system handling performance is steady-states cornering. It refers to an idealized situation that vehicle is driving on a fixed-radius circle with a constant steering angle. Small variations of steering angle due to external disturbance such as wind and frictional coefficient will be neglected for oversteer and understeer will be neglected. Comparing Ackermann steering angle when driving on the circle with the same radius R:

$$\begin{aligned} \delta_{ack,kin} &= \delta_{ack,dyn} \\ \delta_{kin} = \delta_{dyn} - \alpha_f + \alpha_r &\rightarrow \delta_{dyn} = \delta_{kin} + (\alpha_f - \alpha_r) \end{aligned} \tag{11}$$

A dynamic bicycle model is said to be neutrally steering if its steering angle $\delta_{dyn} = \delta_{kin}$. So front and rear slip angles are equal. If $\alpha_f = \alpha_r$ the rear wheel has a larger slip angle, and the vehicle tends to oversteer and

requires a smaller δ_{dyn} than neutral steer to stay on the circle. If the vehicle understeer, it requires a larger than neutral steering angle.

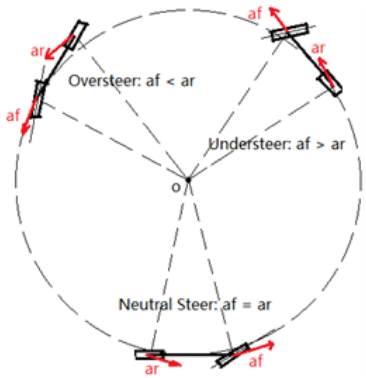

Figure 6: Understeer & Oversteer vs Slip Angle

It is observed that vehicle slip angle co-relates with the lateral acceleration. For vehicle driving at low speeds or corner with large radius, a small lateral acceleration generates small slip angle on all tires, the vehicle tends to stay in neutral steer. As lateral acceleration increases, the slip angle on all tires grows, resulting in understeer and oversteer. To quantitatively measure these behaviors, understeer gradient is defined as the rate of change of under/oversteer with lateral acceleration.

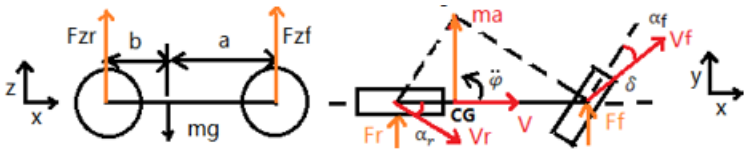

Figure 7: Understeer & Oversteer vs Slip Angle

As shown in Figure 7, given a linear dynamic bicycle model with small steering angel on steady states cornering. Assuming linear tire properties, the lateral force on vehicle is perpendicular to its wheelbase, and cornering stiffness C_f, C_r is linearly proportional to normal force $F_{z,fr}$. Tire forces can be calculated by:

$$F_{y,f} = C_f * \alpha_f, F_{y,r} = C_r * \alpha_r \tag{12}$$

Writing force and moment equilibrium in X-Z plane:

$$\begin{aligned} \sum F_z = 0, F_{zf} + F_{zr} = mg \\ \sum M_{i,y} = 0, bF_{zr} - aF_{zf} = 0 \end{aligned} \tag{13}$$

As a result:

$$F_{zf,zr} = \frac{(a,b)}{L} mg = W_{f,r} mg \tag{14}$$

Writing centripetal force and angular moment equilibrium in X-Y plane:

$$\begin{aligned} m(-\frac{v_x^2}{R}) = -(F_f + F_r) \\ I_z \ddot{\phi} = bF_r - aF_f = 0 \end{aligned} \tag{15}$$

Stationary rotation holds when yaw acceleration $\ddot{\phi}$=0, and lateral force can be written as:

$$\begin{aligned} m(-\frac{v_x^2}{R}) = -(F_f + F_r) \\ I_z \ddot{\phi} = bF_r - aF_f = 0 \end{aligned} \tag{16}$$

Substitute the linear tire force model, the front and rear slip angle can be solved:

$$\begin{aligned} m(-\frac{v_x^2}{R}) &= -(F_f + F_r) \\ I_z\ddot{\phi} &= bF_r - aF_f = 0 \end{aligned} \tag{17}$$

Plug tire slip angle expressions into dynamic steering angle equations:

$$F_{y,f} = C_f * \alpha_f, F_{y,r} = C_r * \alpha_r \tag{18}$$

If the factor $(\frac{W_f}{C_f} - \frac{W_r}{C_r}) > 0$, the required dynamic steering angle increases with longitudinal speed, which matches to understeering behavior of the vehicle. For $(\frac{W_f}{C_f} - \frac{W_r}{C_r}) < 0$,the steering angle decreases with the speed, matching oversteer behavior. Hence the term is named understeer gradient K. From the equation also describes lateral acceleration $a_{lat} = \frac{v_x^2}{R}$,that is required for the vehicle to drive on a circle. Plug in: $W_{f,r} = \frac{a}{L} or \frac{b}{L}$, understeer gradient K can be rewritten as: $K = \frac{b}{LC_f} - \frac{a}{LC_r} = \frac{bC_r - aC_f}{LC_fC_r}$. It can be observed from numerator that $bC_r > aC_f$ results in a non-negative K, equivalents to vehicle neutral steer and understeer. Condition $bC_r < aC_f$results in negative K and vehicle oversteer. Recall the yaw dynamic analysis in section (2.2) where effects of $C = \frac{mv_x^2(b^2C_r) - a^2C_f) + C_fC_r(a+b)^2}{mI_zv_x}$ on eigenvalues and stability were discussed. It can be concluded that a vehicle must be understeer or neutral steer to be stable. An oversteer vehicle is only stable up to a threshold velocity and unstable at above.

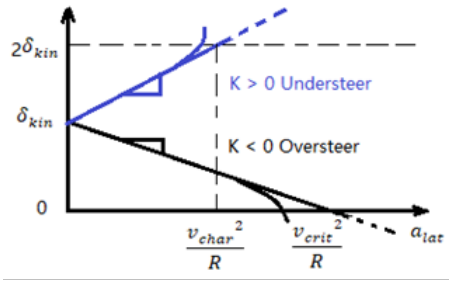

Figure 8: Characteristic Velocity and Critical Velocity

The relation of δ_{dyn} vs a_{lat} was plotted on Figure 8. According to the equation, if the a_{lat}=0, δ_{dyn}=δ_{kin}. For understeer vehicle, the gradient K is positive, hence the relation between steering angle to a_{lat} should be upward sloping. The characteristic velocity is defined as the speed to which dynamic steering angle δ_{dyn}=$2\delta_{kin}$. For oversteer vehicle, the gradient is negative hence the line is downward sloping. At a point that dynamic steering angle passes 0, its corresponding velocity is defined as the critical speed.

In real world the graph can be obtained from experiments, during which vehicle will be driven on circle with different radius at various speeds. Lateral acceleration and steering angle at the steady states will be recorded. Data from the linear region where vehicle speed is low enough should be used to determine the value of understeer gradient K. Vehicle with torque distribution algorithm should show a larger linear region and higher characteristic speed. A successful algorithm should yield to a nearly consistent gradient at low/high speeds. Details of experiments can be referred to ISO4138.

2.4 Torque Vectoring & Traction Control

2.4.1 Slip Ratio

To refine vehicle model for dynamic control, slip ratio is introduced as a control variable. On a RWD dual motor powertrain, slip on front tire is negligible, vehicle speed is estimated by the average of front wheel speeds

omega. Slip ratio is calculated as:

$$\lambda = \frac{V_{wheel} - V_{vehicle}}{V_{vehicle}} = \frac{\omega R_w - V_{vehicle}}{V_{vehicle}} \tag{19}$$

RPM are measured by hall-effect sensor on wheel. $\omega R_w > V$ indicates wheels spinning, which occurs when driving on puddle surface with low frictional coefficient. Slip ratio for maximum spinning equal to 1. $\omega R_w > V$ occures when wheels are skidding during deceleration. In case of heavy panic braking, $\omega R_w \approx 0$ but $V > 0$, so wheels lock-up and slip ratio tends to be -1. An ideal slip ratio is about 0.1 - 0.2 to maximize traction on dry asphalt.

2.4.2 Slip Angle

Slip angle α is estimated individually by steering angle of the wheel δ, track width T and front and rear wheelbase a & b. Model also requires IMU measurements yaw rate ϕ'.

$$\begin{aligned} \alpha_{fl} &= \delta_{fl} - atan(\frac{v_y + a\phi'}{v_x - \frac{T_f}{2}\phi'}) \\ \alpha_{fr} &= \delta_{fr} - atan(\frac{v_y + a\phi'}{v_x + \frac{T_f}{2}\phi'}) \end{aligned} \tag{20}$$

$$\begin{aligned} \alpha_{fl} &= (\frac{-v_y + b\phi'}{v_x - \frac{T_r}{2}\phi'}) \\ \alpha_{fr} &= (\frac{-v_y + b\phi'}{v_x + \frac{T_r}{2}\phi'}) \end{aligned} \tag{21}$$

2.4.3 Tire Force Estimation

Magic Formula of Pacejka is adopted to analyze tire forces. A set of equations interpolate longitudinal and lateral frictional coefficients with slip ratio λ and slip angle α.

$$\begin{aligned} \mu(\lambda) &= D * sin(C * atan(B\lambda - E(B\lambda - atan(B\lambda)))) \\ \mu(\alpha) &= D * sin(C * atan(B\alpha - E(B\alpha - atan(B\alpha)))) \end{aligned} \tag{22}$$

Factors B, C and D are stiffness, curvature, and peak factor of the curve, which are determined by tire vertical loads and camber angles, respectively. The coefficients further determine forces on two directions with respect to normal forces. With tire testing data from Calspan, the characteristic of frictional coefficient can be interpolated. From Figure 9 it can be observed that Formula tire can provide maximum 900 N longitudinal traction forces on dry surface at around $\lambda = 0.20$

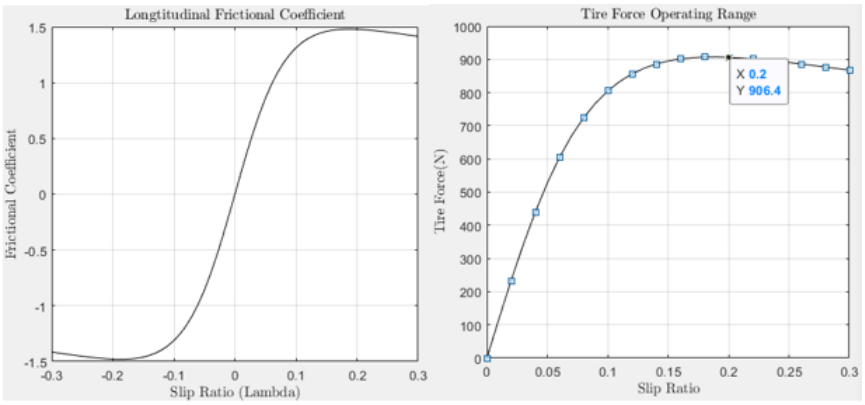

Figure 9: Longitudinal Coefficient and Tire Force

Since the Pacejka formula assumes linear response on vertical and lateral directions, a constant tire damping, it works best in predicting tire behavior under 0.4G lateral acceleration and 5o side slip angle. The longitudinal and vertical load traction can be calculated as:

$$F_t = F_z\mu(\lambda), F_s = F_z\mu(\alpha) \tag{23}$$

Note that it is impossible to maximize tractions on both directions and achieve greatest reaction force simultaneously. Requesting more slip ratio after reaching peak longitudinal $\mu(\lambda)$ will reduce lateral $\mu(\alpha)$. As described by Pacejka, the total traction is limited within a "Frictional Ellipse" given a fixed normal force. From the linear interpolation shown in figures above, we can pick a target slip ratio to maximize traction and calculate lateral force and frictional coefficient based on the circle.

$$\frac{mu(\lambda)^2}{x^2} + \frac{mu(\alpha)^2}{y^2} = 1, \mu(\alpha) = \frac{x\sqrt{y^2 - \mu(\lambda)^2}}{n} \tag{24}$$

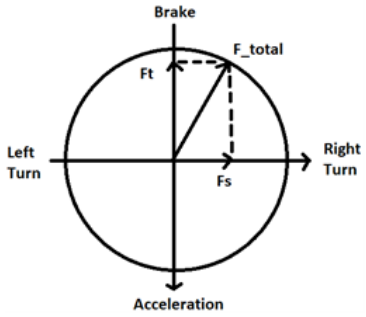

Figure 10: Longitudinal Coefficient at Different Slip Angle Given Friction Ellipse

2.4.4 Body Force Estimation on Four-Wheels

After tire forces are generated, a force and moment equilibrium around CG of four-wheel model can be summarized as:

$$\begin{aligned} F_{x,fl} &= F_{t,fl} * cos(\phi_{fl}) - F_{s,fl} * sin(\phi_{fl}) \\ F_{y,fl} &= F_{t,fl} * cos(\phi_{fl}) + F_{s,fl} * sin(\phi_{fl}) \\ F_{x,fr} &= F_{t,fl} * cos(\phi_{fr}) - F_{s,fr} * sin(\phi_{fr}) \\ F_{y,fr} &= F_{t,fl} * cos(\phi_{fr}) + F_{s,fr} * sin(\phi_{fr}) \end{aligned} \tag{25}$$

$$\begin{aligned} F_{x,rl} = F_{t,rl},\ F_{y,rl} = F_{s,rl} \\ F_{x,rr} = F_{t,rr},\ F_{y,rr} = F_{s,rr} \end{aligned} \tag{26}$$

The differential equation for longitudinal and lateral dynamics can be described as:

$$\begin{aligned} M_v(\dot{v_x} - v_y\phi') = F_{x,fl} + F_{x,fr} + F_{x,rl} + F_{x,rr} \\ M_v(\dot{v_x} + v_y\phi') = F_{y,fl} + F_{y,fr} + F_{y,rl} + F_{y,rr} \end{aligned} \tag{27}$$

Yaw dynamics is a result of torque equilibrium with respect to Z-axis:

$$I_z\phi'' = a(F_{y,fl} + F_{y,fr}) - b(F_{y,rl} + F_{y,rr}) - T_{fl}F_{x,fl} + T_{fr}F_{x,fr} - T_{rl}F_{x,rl} + T_{rr}F_{x,rr} \tag{28}$$

Aerodynamics package regulates down force on the chassis. Their effects are modeled based on air density, vehicle speed, lift and drag coefficient C given by wind tunnel test:

$$\begin{aligned} F_{down,total} = \frac{1}{2}\rho_{air}C_l v_x^2 A \\ F_{drag,total} = \frac{1}{2}\rho_{air}C_d v_x^2 A \end{aligned} \tag{29}$$

2.4.5 Control Design

With the vehicle dynamics modeled in MATLAB Simulink, a PID based nested control loop with compensator is proposed to achieve traction control and torque vectoring. Traction control module aims to keep slip ratio around an optimal operation point λ = 0.18 - 0.25. A feedforward controller predicts maximum torque on the wheel based on optimal slip condition, and a feedback PI controller is used to compensate for model uncertainty.

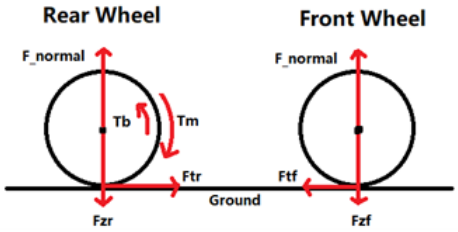

Figure 11: Simplified Half Vehicle Wheel Dynamics

In Straight line acceleration, each rear wheel actuates half the vehicle inertia. Based on Newton's 2nd law:

$$\begin{aligned} \frac{1}{2}mv' &= \frac{1}{2}F_{tr} - \frac{1}{2}F_{drag} \\ v' &= \frac{(F_{tr} - F_{drag})}{m} \end{aligned} \tag{30}$$

Combined with torque equilibrium on a single rear wheel as shown in Figure 11:

$$\begin{aligned} J_w * \omega' &= T_m - T_b - R_w * F_{tr} \\ J_w * \omega' &= T_m - T_b - R_w * F_{tr} \\ J_w * \frac{v'_w}{R_w} &= T_m - T_b - R_w * F_{tr} \\ v'_w &= (T_m - T_b - R_w * F_{tr})\frac{R_w}{J_w} \end{aligned} \tag{31}$$

A relationship of vehicle acceleration and wheel acceleration can be derived for predicting the maximum feedforward torque at the ideal slip ratio:

$$\begin{aligned} \frac{v}{v'_w} &= \frac{(F_{tr} - F_{drag})/m}{(T_m - T_b - R_w * F_{tr})\frac{R_w}{J_w}} = (1 - \lambda_{ideal}) \\ T_{pred} &= \frac{(F_{tr,max} - F_{drag})J_w}{(1 - \lambda_{ideal})} + F_{tr,max}R_w + T \end{aligned} \tag{32}$$

Torque vectoring is achieved by yaw rate estimation. The algorithm tracks steering input and vehicle velocity to estimate an ideal yaw rate that driver wants to achieve:

$$\phi'_{ideal} = \frac{v_x \delta}{L} \tag{33}$$

From real time vehicle states, a maximum available yaw rate is calculated at the peak lateral forces. The maximum yaw rate is estimated based on assumption that vehicle is not drifting. No lateral acceleration, but only centrifugal exists in the model [1]. Since this yaw rate from ideal scenario is likely to exceed max yaw rate in real world, the value 0.95 is set as an empirical safety factor.

$$F_{y,max} = F_{z,fl} * \mu_{fl,peak} * cos(\delta_{fl}) + F_{z,fr} * \mu_{fr,peak} * cos(\delta_{fr}) + F_{z,rl} * \mu_{rl,peak} + F_{z,rr} * \mu_{rr,peak} \tag{34}$$

$$\phi'_{ideal} = 0.95\frac{F_{y,max}}{M_v v_x} \tag{35}$$

For skidpad events, the vehicle drives two laps on a "figure-8" with constant radius. Vehicle reaches steady states in middle of the 1st lap and maintain such dynamics until cornering exit. The max yaw rate in this case maintains constant as:

$$\phi'_{skid} = \frac{v_x}{R} \tag{36}$$

It is reasonable to set ϕ'_{skid} as control target during skidpad event. Once optimal yaw rate is not depending on steering angle, driver may adjust steering angle to achieve a time-saving trajectory: by slightly decreasing steering angle, a larger traction force will be distributed to longitudinal direction, so vehicle speed will increase [1]. During track drive, system sets ϕ'_{ideal} as the control target to achieve driver intended maneuvers unless $\phi'_{ideal} > \phi'_{max}$. A proportional controller distributes torque difference between two rear wheels:

$$\Delta T = K_p(\phi'_{target} - \phi'_{measured}) \tag{37}$$

Oversteer sometimes occurs when driver requests yaw rate drastically at performance limits. Most tractions are distributed on longitudinal direction to achieve high speed. And vehicle tends to slide out due to lack of lateral tractions that maintain angular motion. To fix this, driver commonly releases throttle and applies an opposite steer. In order not to intervene driver's instinct, system compares direction of $\phi'_{measured}$ and ϕ'_{ideal} to detect counter-steer action, and assists vehicle status recovering by applying torque as below:

$$\Delta T_{countersteer} = \Delta T(1 - \frac{|\phi'_{ideal}|}{\phi'_{limit}}),\ \phi'_{limit} = 0.25\ (rad/s) \tag{38}$$

When torque requests from traction control and torque vectoring modules are infused, a logic check is set prior to inverter and motor, such that:

$$\begin{gathered} \Delta T = T_R - T_L \\ max(T_R, T_L) = min(T_{request} - T_{TCmax(R,L)}) \end{gathered} \tag{39}$$

The combined system diagram is shown below:

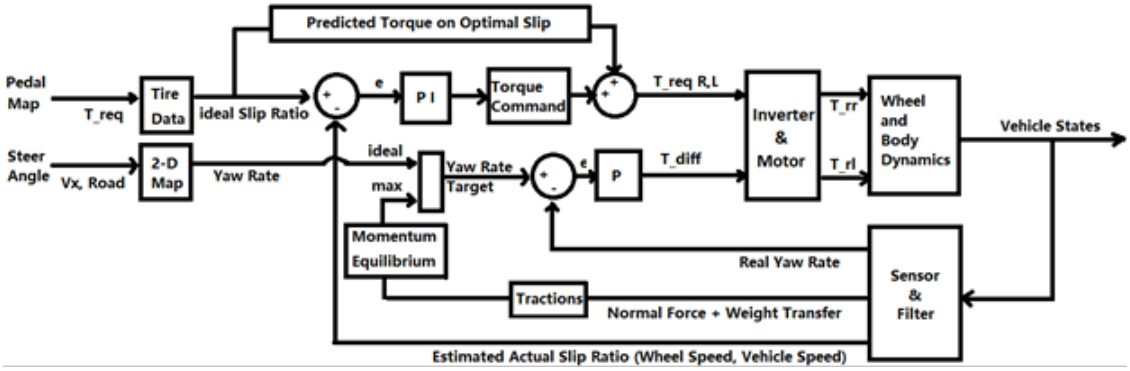

Figure 12: Feedforward-Feedback Control Architecture

2.4.6 Results

Vehicle dynamics model and controller were verified using MATLAB Simulink. A stability analysis was performed on traction control system under the straight-line acceleration scenario. Assuming steady states, an optimal torque request was calculated on ideal slip ratio operating points, along with the corresponding wheel speeds and yaw rates. Selecting $Y = [V\ \omega\ \lambda\ T_w]^T$ as controlled variables and linearized a discrete traction control dynamics around: V=35 m/s, ω=180 rpm, λ=0.18 and T_w=Tmax. A state-space representation was solved from Jacobian matrix:

$$\begin{gathered} \frac{d}{dt}\begin{bmatrix} V \\ \omega \\ \lambda \end{bmatrix} = \begin{bmatrix} 0.9953 & 0.0 & 0.0534 \\ 0.0 & 0.9903 & -9.9627 \\ -0.0308 & 0.0064 & -0.0657 \end{bmatrix}\begin{bmatrix} V \\ \omega \\ \lambda \end{bmatrix} + \begin{bmatrix} 0 \\ 0.0653 \\ 0.0004 \end{bmatrix} T_w \\ C = [0\ 0\ 1],\ D = [0] \end{gathered} \tag{40}$$

Figure 13 indicated that slip ratio oscillates under step torque input in open-loop. When implementing proportional control, steady states error existed. With PI compensator, slip ratio quickly converged to λ_{ideal}=0.18 with τ = 0.02s and $T_{Settle,98}$=2.65 s without overshoot due to large Ki values. Such behavior could be explained from pole-zero map: on a discretized complex plane system had positive real poles on RHP. The PI controller relocated real poles closer to unit circle, resulting in a slower rise time. Since all poles were located within circle at sampling time T = 0.01s, systems were stable and converge to steady states overtime. Larger K_p and K_i values can be fine-tuned for faster response.

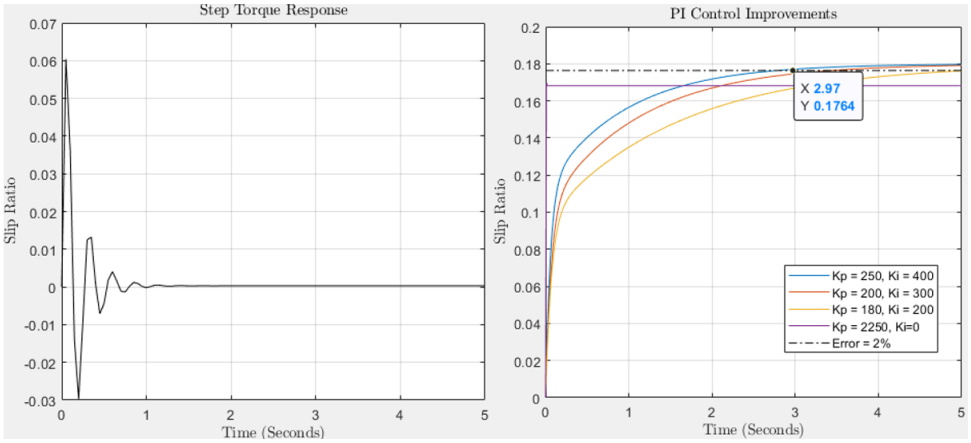

Figure 13: Slip Ratio Response Open-Loop vs PI Control

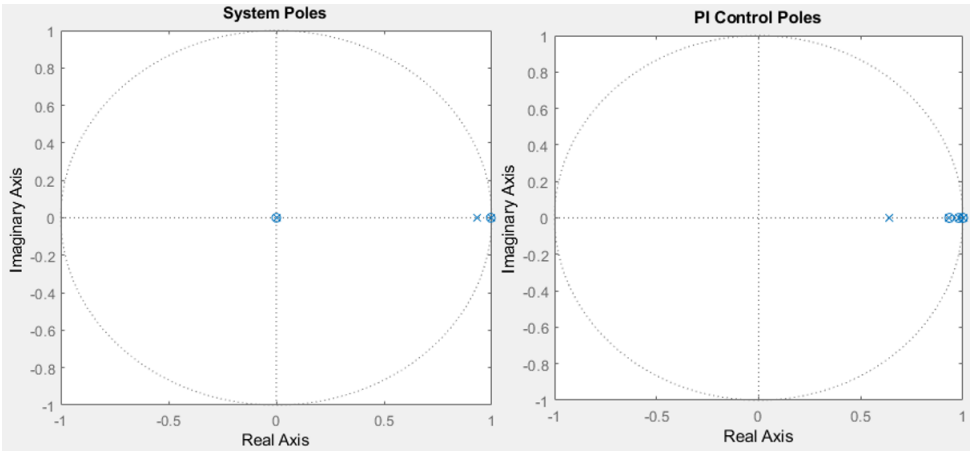

Figure 14: Pole-Zero Map of System with PI Controller

Effectiveness of traction control system could also be validated from vehicle testing data. Figure 15 showed a scenario that vehicle encountered a bump or puddle during straight line acceleration events. The rear left wheel lost traction and quickly spinned out at 27s. Upon detecting the surge in slip ratio, system reduced torque output by 50% as shown in Figure 16. Within 0.5 second the vehicle recovered its status. The torque output data indicated a 50% torque increase due to the feedforward torque prediction (32). Higher top speed and acceleration were also observed on vehicle with traction control enabled, confirming the performance gain.

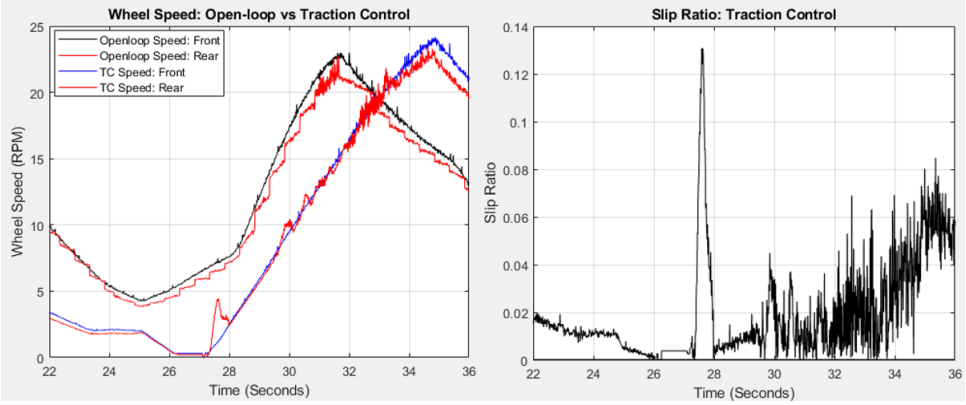

Figure 15: Wheel Speed and Controlled Slip Ratio in Straight Line Acceleration

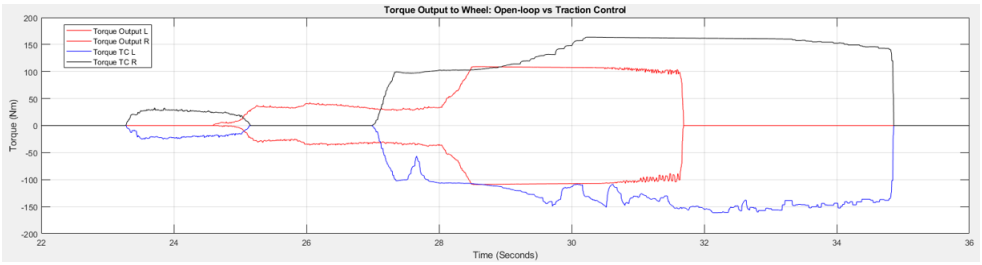

Figure 16: Motor Torque Output Comparison

Cornering dynamics was also simulated based on linearized bicycle model (3) described in section 2. Figure 17 shows the lateral acceleration and yaw rate of vehicle under a double lane change scenario, in which driver input step steers to left, right and recovering. Due to highly stiffed suspension components, all responses had short settling time within 0.3s. Yaw rate ranged from 60 to 100 rad/s^2, increasing proportional to step magnitudes. Lateral accelerations showed an inverse relation to vehicle velocity because less lateral tractions were available based on frictional ellipse. It was also observed that lateral acceleration responses tended to overshoot at higher velocity, matching up with the oversteer properties described in section 2.3.

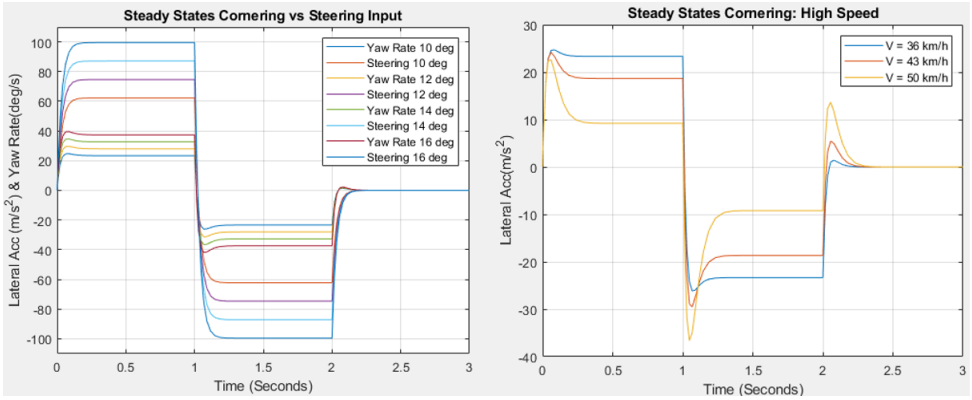

Figure 17: Lateral Dynamics with Step Steer on Open Loop

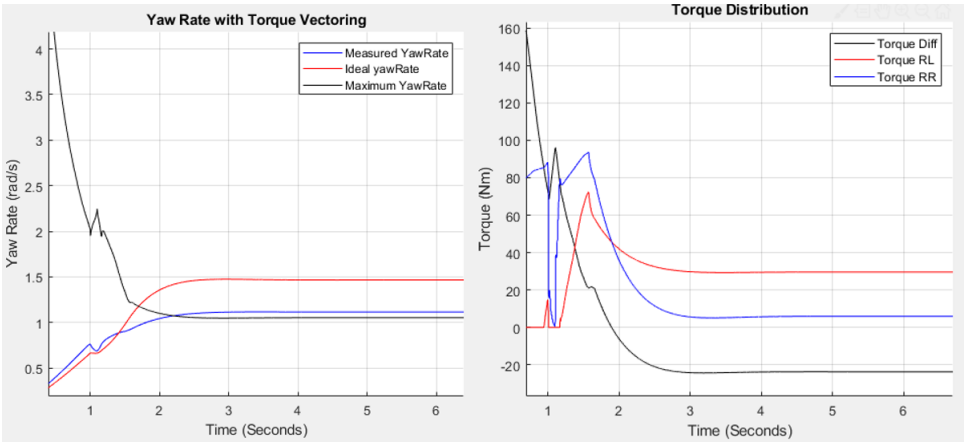

Figure 18: Yaw Rate and Torque Distribution in with Torque Vectoring

A circular driving on constant radius was simulated as the second lap of skid-pad event. Assuming driver input a full throttle and constant steering angle at 10 degrees [1]. From Figure 18, ϕ'_{max} was high at the beginning due to small velocity on denominator (33). A large ΔT request was generated but ignored since it was larger than traction control threshold $T_{TCmax(R,L)}$from Equation (39). A discrete impulse was sent to rear wheels as perturbations. With both controls activated, vehicle lost traction upon surge of slip ratio at 1 second but quickly recovered by cutting torque request. Since the outer wheel was under higher torque, vehicle had a tendency of oversteer, which was corrected by a ΔT = -20 Nm at steady states. As a result, the measured yaw rate converged to maximum possible yaw rate, indicating cornering maneuver was at the vehicle performance peak. Note that under a single proportional controller, the steady states error between $\phi'_{measured}$ and ϕ'_{ideal} was not be corrected. With integral control being applied, system would request additional control effort that resulted in tractions beyond tire limits, so that vehicle would spin.

3 MPC for Autonomous Driving

3.1 Overview

Model predictive control for autonomous driving aims to produce obstacle-free trajectory from vehicle's current position to a local target, based on road condition, vehicle dynamics and environmental information measured by perception system. Trajectory planning can be completed upon object detection or after map building. One big advantage of MPC is the multiple boundary conditions introduced to controlled variables. At lower velocity, conditions from vehicle kinematics has higher effects; as velocity increases, dynamic force interactions will play a more important role. Shouwenaars, How and Feron (2004) proposed a receding horizon path planning method that predicts vehicle trajectories with a library of circle arcs [13]. The method provided a safety measurement to obstacle but did not count for the changing radius in cornering, hence tracking failure might occur at high speed. Cong, An and Chen (2012) improved principles of receding-horizon optimization. Geometric constrains were set on starting poses and least cornering radius to compensate for position and vehicle heading errors [16].

This section introduces a general workflow of path tracking design including model linearization, discretization, prediction horizon setting and control optimization.

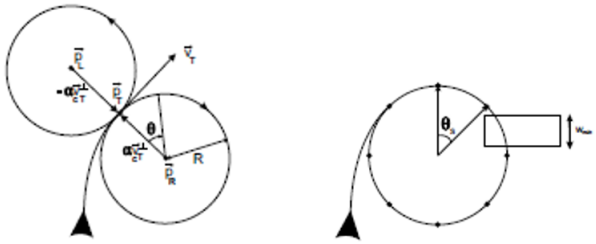

Figure 19: Safe Trajectory Library from Shouwenaars (2004)

3.2 Vehicle Model for MPC

In traditional vehicle control, the model should capture system dynamics as detailed as possible, so that controller can be optimized for transient responses. However, research of Liu J, Jayakumar P, Overhold J L, et al. indicated that a MPC with 2-DOF vehicle model had similar tracking capability to 14-DOF model under the same boundary conditions [15]. Since a high-fidelity model introduced significant time complexity in computation, study of MPC should consider a simplified vehicle model with boundary conditions that emulated realistic operating points and physical limits.

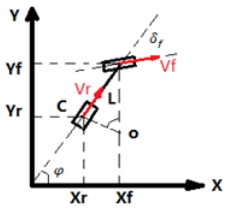

Figure 20: Kinematic Bicycle Model for MPC

The kinematic bicycle model was adopted due to reason above. Vehicle positions and yaw angle were controlled as states $\xi = [X\ Y\ \phi]^T$, using wheel speed and steering input of rear wheel $u = [v_r\ \delta_f]^T$. Assuming instantaneous radius is equal to road curvature, vehicle had CG at C and $v_r = v_x$ at a low speed. The following

equation of motions were written:

$$\begin{aligned} v_f cos(\delta_f) = v_r,\ v_f sin(\delta_f) = v_y \\ v_y = v_r tan(\delta_f),\ \phi' = v_f \frac{tan(\delta_f)}{L} \end{aligned} \tag{41}$$

A nonlinear state space was derived:

$$\frac{d}{dy}\begin{bmatrix} X \\ Y \\ \phi \end{bmatrix} = \begin{bmatrix} cos(\phi) \\ sin(\phi) \\ 0 \end{bmatrix} v_r + \begin{bmatrix} 0 \\ 0 \\ 1 \end{bmatrix} \phi' = \begin{bmatrix} cos(\phi) \\ sin(\phi) \\ \frac{tan(\delta_f)}{L} \end{bmatrix} \tag{42}$$

Apply linear approximation. Assuming a reference system passed waypoints on ideal trajectory so that states and control input of reference system at any time can be measured:

$$\xi'_{ref} = f(\xi_{ref}, u_{ref}) \tag{43}$$

Errors between measured system and referenced system can be derived as:

$$\xi_e = \xi - \xi_r = \begin{bmatrix} X - X_r \\ Y - Y_r \\ \phi - \phi_r \end{bmatrix}, u_e = u - u_r = \begin{bmatrix} v_r - v_{ref} \\ \delta_f - \delta_{ref} \end{bmatrix} \tag{44}$$

Solving a 1st order Tayler Series expansion at reference trajectory (ξ_{ref}, u_{ref}):

$$\xi' = f(\xi_{ref}, u_{ref}) + \frac{df}{d\xi}(\xi - \xi_r) + \frac{df}{du}(u - u_r) \tag{45}$$

Subtracted equation (43) from equation (45), the state space of vehicle error states was derived:

$$\xi_e = \xi - \xi_r = \frac{df}{d\xi}(\xi - \xi(r)) + \frac{df}{du}(u - u_r) \tag{46}$$

$$\xi'_e = A\xi_e + Bu_e \tag{47}$$

Where A,B should be solved as Jacobian matrix $J_f(x_1\ \dots\ x_n) = \begin{bmatrix} \frac{dy_1}{dx_1} & \cdots & \frac{dy_1}{dy_n} \\ \vdots & \ddots & \vdots \\ \frac{dy_m}{dx_1} & \cdots & \frac{dy_m}{dy_n} \end{bmatrix}$, as a result:

$$\frac{d}{dy}\begin{bmatrix} X_e \\ Y_e \\ \phi_e \end{bmatrix} = \begin{bmatrix} 0 & 0 & -v_r sin(\phi_r) \\ 0 & 0 & v_r cos(\phi_r) \\ 0 & 0 & 0 \end{bmatrix} \begin{bmatrix} cos(\phi_r) & 0 \\ sin(\phi_r) & 0 \\ \frac{tan(\delta_f)}{L} & \frac{v_r}{Lcos^2(\delta_f)} \end{bmatrix} \begin{bmatrix} v_{r,e} \\ \delta_{f,e} \end{bmatrix} \tag{48}$$

The state space was further discretized with Forward-Euler method, where A=(I+TA),B=(TB). Given:

$$\begin{aligned} \xi_e = \frac{\xi_e(k+1) - \xi_e(k)}{T} = A\xi_e(k) + Bu_e(k) \\ \xi_e(k+1) = A(k)\xi_e(k) + B(k)u_e(k) = (I + TA)\xi_e(k) + (TB)u_e(k) \end{aligned} \tag{49}$$

As a result, a linear time variant states-space for vehicle state-error dynamics was derived:

$$\frac{d}{dy}\begin{bmatrix} X_e \\ Y_e \\ \phi_e \end{bmatrix} = \begin{bmatrix} 1 & 0 & -Tv_r sin(\phi_r) \\ 0 & 1 & Tv_r cos(\phi_r) \\ 0 & 0 & 1 \end{bmatrix} \begin{bmatrix} Tcos(\phi_r) & 0 \\ Tsin(\phi_r) & 0 \\ T\frac{tan(\delta_f)}{L} & T\frac{v_r}{Lcos^2(\delta_f)} \end{bmatrix} \begin{bmatrix} v_{r,e} \\ \delta_{f,e} \end{bmatrix} \tag{50}$$

3.3 Prediction & Control

Based on equation (49), setting prediction horizon Np = 4 and control horizon Nc = 3, the effect of control effort $u_e(k)$ to vehicle states and outputs within horizon should be:

$\xi_e(k+1) = A\xi_e(k) + Bu_e(k)$
$\xi_e(k+2) = A^2\xi_e(k) + ABu_e(k) + Bu_e(k+1)$
$\xi_e(k+3) = A^3\xi_e(k) + A^2Bu_e(k) + ABu_e(k+1) + Bu_e(k+2)$
$\xi_e(k+4) = A^4\xi_e(k) + A^3Bu_e(k) + A^2Bu_e(k+1) + ABu_e(k+2) + Bu_e(k+3)$
Equations could be summarized as a general form:

$$
\begin{gathered}
Y = \bar{A}\xi_e(k) + \bar{B}U(k) \\
Y = \begin{bmatrix} \xi_e(k+1) \\ \vdots \\ \xi_e(k+N_p) \end{bmatrix} \quad A = \begin{bmatrix} A \\ \vdots \\ A_p^N \end{bmatrix} \quad \xi_e(k) = \begin{bmatrix} X_e \\ Y_e \\ \phi_e \end{bmatrix} = \begin{bmatrix} X - X_r \\ Y - Y_r \\ \phi - \phi_r \end{bmatrix} \\
B = \begin{bmatrix} B & 0 & 0 & 0 \\ AB & B & 0 & 0 \\ A^2B & AB & B & 0 \\ \vdots & \vdots & \vdots & \vdots \\ A^{N_p-1}B & A^{N_p-2}B & \dots & A^{N_p-N_c-1}B \end{bmatrix} U(k) = \begin{bmatrix} u_e(k) \\ u_e(k+1) \\ u_e(k+N_p) \end{bmatrix}
\end{gathered}
\tag{51}
$$

To find the optimal control effort at each step, a quadratic cost function was formulated. The target was to quickly converge vehicle states Y to reference states Y_{ref} with a minimum effort U at each time. In this process, the weighted square sum of each variable should be minimized, so the problem could be solved as quadratic optimization. A general form of cost functions can be derived:

$$
J = \sum_{j=1}^{N} (Y - Y_{ref})^T Q (Y - Y_{ref}) + U^T R U \tag{52}
$$

The Q and R matrix penalized system's tracking capability and control smoothness, respectively. Defined a term:

$$
\begin{gathered}
E = \bar{A}\xi_e(k) - \bar{A}\xi_e(k)_{ref} = \bar{A}\xi_e(k) - Y_{ref} \\
Y - Y_{ref} = \bar{A}\xi_e(k) + \bar{B}U(k) - Y_{ref} = E + \bar{B}U(k)
\end{gathered}
\tag{53}
$$

Rewrote the cost function with a single variable U, ET QE was not controllable:

$$
\begin{aligned}
J &= (E + \bar{B}U)^T Q (E + \bar{B}U) + U^T R U && (54) \\
&= E^T Q E + (\bar{B}U)^T + 2E^T Q(\bar{B}U) + U^T R U && (55) \\
&= U^T \bar{B}^T Q \bar{B} U + 2R^T Q \bar{B} U + U^T R U && (56)
\end{aligned}
$$

To optimize U with QP, minimize:

$$
\begin{gathered}
J = U^T(\bar{B}^T Q \bar{B} + R)U + 2E^T Q \bar{B} U = \frac{1}{2} U^H U + f^T U \\
s.t. \begin{bmatrix} v_{min} \\ \delta_{min} \end{bmatrix} \leq U \leq \begin{bmatrix} v_{max} \\ \delta_{max} \end{bmatrix}
\end{gathered}
\tag{57}
$$

The optimal U for one step further was selected and implemented to wheel speed and steering. As vehicle states was changing, a new set of optimums U had to be predicted at each time interval and the control loop could be summarized as:

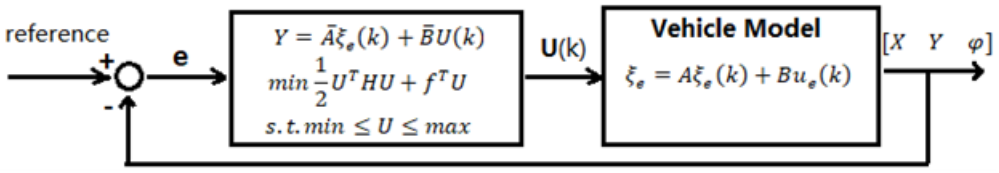

Figure 21: MPC Feedback Control Loop

Based on Jianwei Qiu (2014) [11], quadprog solver in MATLAB was applied to generate results in Figure 22. Red-dot trajectory indicated that vehicle was able to track straight line closely at all speeds. Blue line was generated as the vector of U at each time steps. An offset of 1.5 m and heading angle 60 degrees were manually introduced assuming vehicle could not start right on the track center. It was observed from Figure 22 that large speed and steering was required at beginning to correct the trajectory. With a higher speed or larger heading error, trajectory might overshoot but eventually converge.

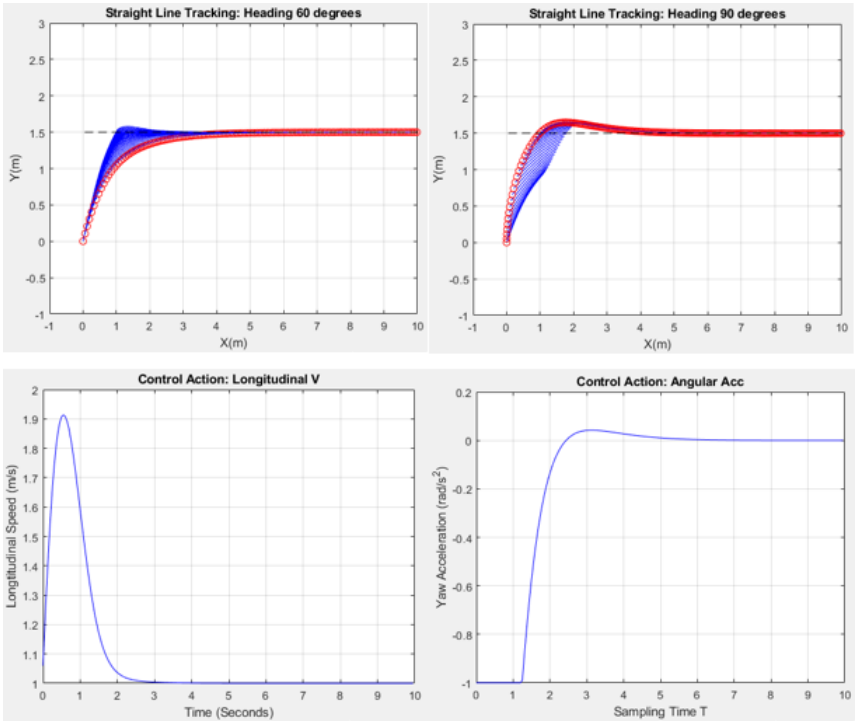

Figure 22: Trajectory Tracking for Straight Line

On curved trajectory, error occurred with naive controller at higher speed. Index of Q matrix was set as higher priority to penalize large deviation from reference track. Hence on Figure 23, a spike of 1.7 rad/s yaw rate was requested from steering to correct Y position error at T = 1 second. Algebraic-Riccati Equation could be solved to define Q matrix. It was also applicable to tune the index's order of magnitude to be (1/error). For example, $Q_X = Q_Y = 100$ was expected to bring position error down to 0.01m. R matrix should be tuned for smoother control effort with a trade-off on position.

Note that a longer prediction and control horizon were beneficial for performance only below a threshold. Time complexities of optimizations should be evaluated in code. From simulation a bifurcation of trajectories was observed in the end. One possible reason was that the last waypoint had been detected at X = 7m, so all trajectories were planned towards the point when approaching. Such behavior might not affect vehicle maneuver and should not exist on a close-loop track map. For next iteration effects of time should be incorporated to improve the tracking precision.

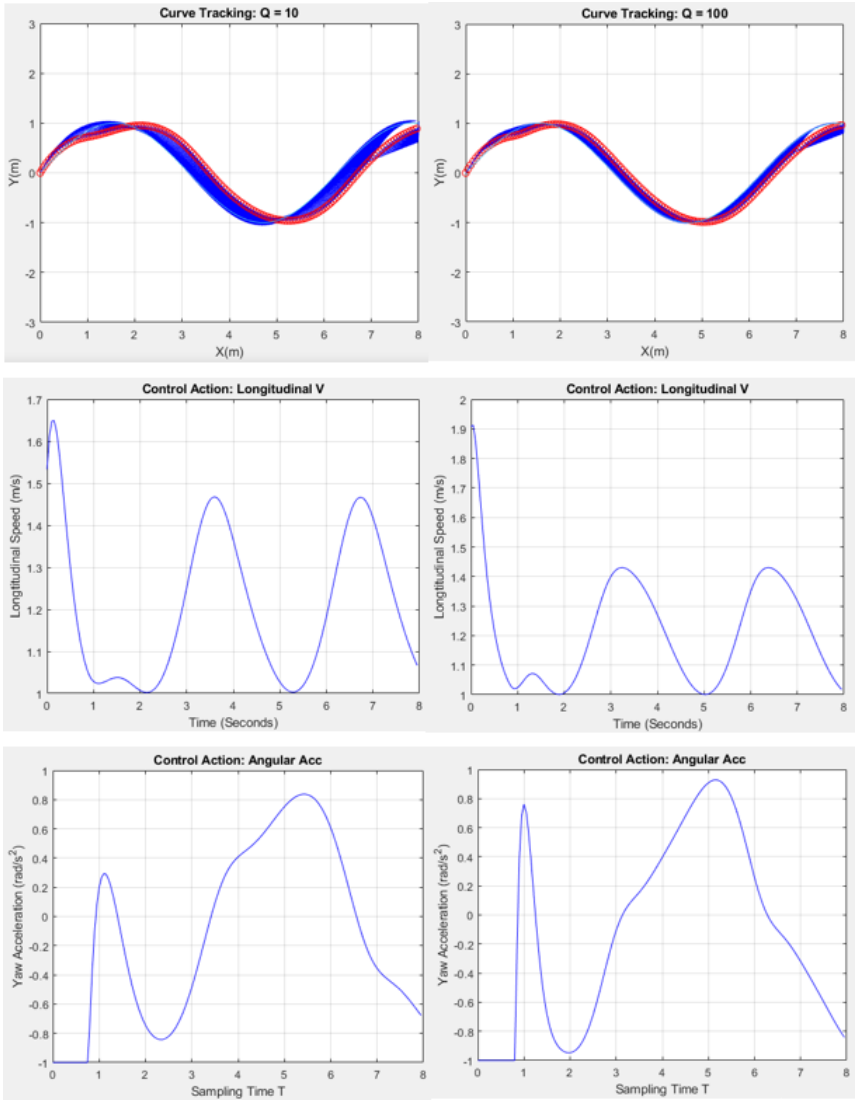

Figure 23: Trajectory Tracking Curve with Penalized Error State

4 Hardware Implementation

4.1 System Identification

An experimental method to determine motor dynamic characteristic was system identification. Multiple torque commands were applied to motor and corresponding steady states rotational speeds were measured. With linearity examined, slopes of the fitting lines were the damping coefficients of motors. As shown in figure, damping coefficients were 0.1595 on the left and 0.1997 on the right. The difference was a result of manufacturing quality. Moreover, an impulse response test could determine the motor system bandwidth. Motors were first driven to a constant torque output. Current, voltage, RPM and torque data were recorded as soon as torque commends stepped to zero and torque output ramped down. Given the bode plot of this process, motor transfer functions could be established accordingly.

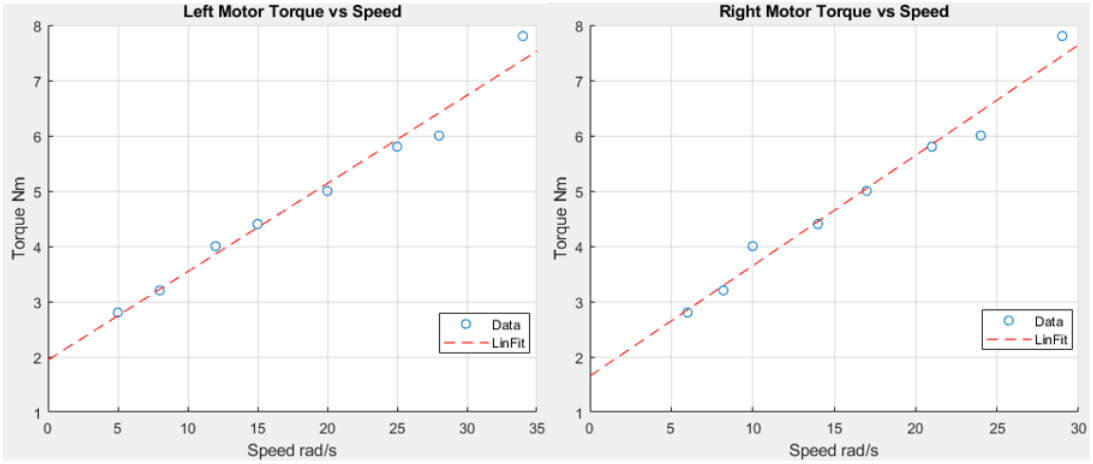

Figure 24: Left and Right Motor Torque vs Speed Curve

Analytical method of motor modeling was enabled by MATLAB Simulink. It was an open option to either establishing Faraday's equation, magnetic link, and EMF in a d-q coordinate for 3-phase induction motor, or tuning parameter from the existing toolbox. A SPWM inverter outputs current prior to the motor, which facilitates the evaluation of energy consumption. Subsystem should output torque response corresponding to request, and RPM response as an inverse relation due to $power = torque \times rpm$ relation.

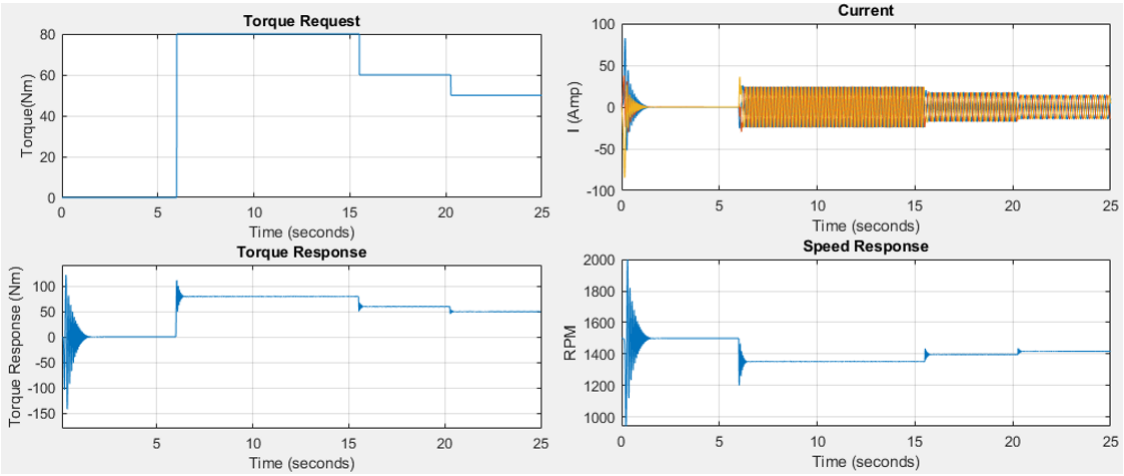

Figure 25: 3-Phase AC Motor Response in Simulink

4.2 Pedal Map

Driver requests vehicle acceleration by throttle pedal. The position will be measured in voltage signal with two potentiometers, and control system mapped pedal inputs to power request through pedal map. The map was a 3D look-up table output motor torque percentage given a throttle percentage through ranges of speed. Some governing equation of pedal – speed – torque relations are:

$$\begin{aligned} T_{command} &= T_{max,90Nm} \times throttle\% \\ Power(kW) &= T_{out,Nm} \times RPM \\ T_{Regen} &= 20\% \times T_{max,90Nm} \end{aligned} \tag{58}$$

At low speed, high gain of acceleration was expected for small amount of pedal input, so speed profile curvature was intentionally increased. At higher speed the slope was decreased since drastic change in power output

would result in unpredictable handling behavior, hence making high speed maneuver dangerous.

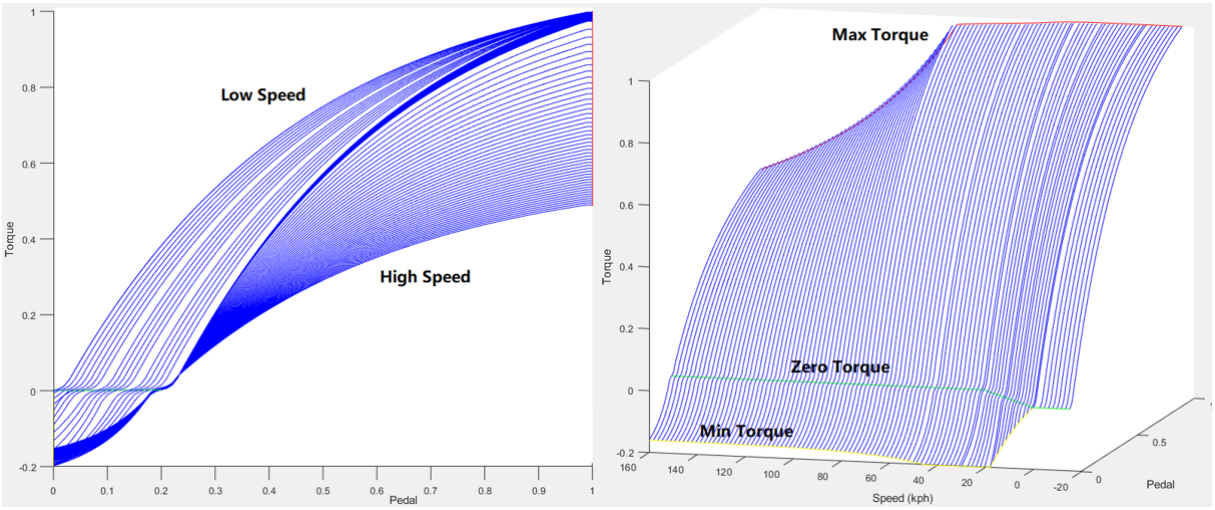

Figure 26: Pedal Map with Max, Zero and Min Torque line

There are three important line in the map: max torque line, zero torque line and minimum toque line. Max torque line was defined the full power output with restriction on motor parameters, competition rule and energy trade-off. Zero torque line defined torque output when driver barely step on throttle and regenerative braking not activated. Min torque line was designed based on -20% regenerative torque, and the value was set empirically given maximum allowable current.

4.3 IMU

Formula T31 vehicle used VectorNav VN-300 dual-antenna GNSS/INS odometry. The primary purpose was to measure vehicle acceleration and speed on X and Y axis using accelerometer, yaw and roll angular rate. Although the industrial grade MEMS device contained GPS and magnetic compensation, offshore IMU without calibration could produce large, accumulated error after minutes of operation. In this section, an error model regarding misalignment, fixed bias and scale factor was explained together with calibration process.

4.3.1 Error Model

There are three major characteristics of IMU: bias, scale-factor error and misalignment errors. Biases b^a and b^g (for accelerometer and gyroscope), are measurement error exist regardless of acceleration or rate. It could be further broken down to fixed bias, stability and instability bias [9]. Stability bias change randomly from every power-up, it would comply to ambient thermal condition in each run. Instability bias can be modeled as a random process over time. Fixed bias contributed largely to measurement error. It could be calibrated as an offset due to deterministic nature in physics. The bias determined will be added or subtracted from each axis in unit of mg (10^{-3} gravity).

Scale-factor error a^S and ω^S (for accelerometer and gyroscope) describe how acceleration or angular rate output correspond to input. The error was deterministic due to MEMS sensor manufacturing quality and could be modeled in linearity. The scale factor shall be calibrated using multiplication on each axis, after bias was determined. The factor was unit-less or in part per million (ppm).

Due to imperfect manufacturing and installation, sensor coordinate frame could be misaligned with IMU chassis frame. Measurements on sense-axis would be inaccurate due to force from the other axis. The misalignment errors were in degree or radius. For accelerometer and gyro, the effect of scale factor and misalignment frame

was modeled in matrices form:

$$M_a = \begin{bmatrix} a_x^s & m_{xy}^a & m_{xz}^a \\ m_{yx}^a & a_y^s & m_{yz}^a \\ m_{zx}^a & m_{zy}^a & a_z^s \end{bmatrix}, M_g = \begin{bmatrix} \omega_x^s & m_{xy}^a & m_{xz}^a \\ m_{yx}^a & \omega_y^s & m_{yz}^a \\ m_{zx}^a & m_{zy}^a & \omega_z^s \end{bmatrix} \tag{59}$$

Ignored gyroscope's g-sensitivity and assumed white noise on both sensors averaged out over time, calibrated measurements of accelerometer and gyroscope can be written as:

$$\begin{aligned} Acc_{out} &= (I_{3\times3} + M_a)Acc_{measured} + b^a \\ Gyro_{out} &= (I_{3\times3} + M_g)Acc_{measured} + b^g \end{aligned} \tag{60}$$

4.3.2 Calibration Method

To determine bias, scale-factor, and misalignment of 3-axis on both accelerometer and gyroscope, 6-point tumble test was performed. A well-aligned horizontal and vertical surface needed to be prepared. The IMU will be placed at six different orientations, with each sense-axe vertically aligned to gravity (positive and negative). If time allows, the device shall be placed at initial position long enough (3 - 5 minutes) so that thermal condition came to steady states. At each position, it was recommended that user took 50 - 200 samples, so that data was not significantly affected by noise, and at the same time free of non-deterministic error. Parameters will be calculated based on measured values.

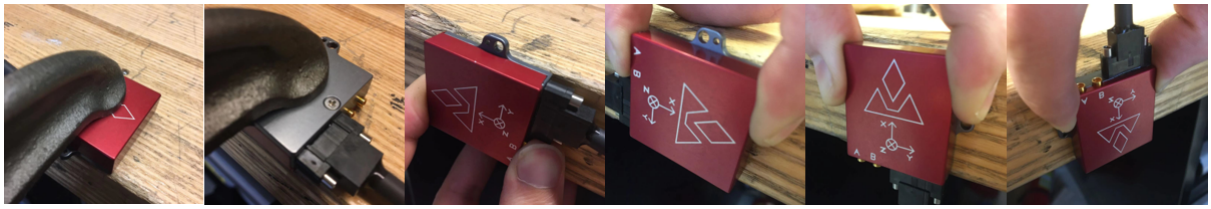

Figure 27: 6-Point Tumble Test Orientation

Measurement data was shown in Table 1:

Align to:	Positive X-axis	Gravity Y-axis	m/s^2 Z-axis	Negative X-axis	Gravity Y-axis	m/s^2 Z-axis
X-sense	9.78837	0.184784	-0.36446	-9.81679	-0.16743	-0.34155
Y-sense	-0.41017	9.789671	-0.3337	0.064814	-9.81114	-0.34862
Z-sense	0.034661	0.089586	9.541856	-0.07384	-0.1134	-10.0133

Figure 28: 6-Point Tumble Test Data

Accelerometer fixed bias vector was averaged from gravity aligned axis measurements:

$$b_a = \frac{1}{2}\begin{bmatrix} Acc_x^+ + Acc_x^- \\ Acc_y^+ + Acc_y^- \\ Acc_z^+ + Acc_z^- \end{bmatrix} = \begin{bmatrix} -0.014211 \\ -0.010735 \\ -0.235705 \end{bmatrix} \tag{61}$$

Accelerometer scale-factor matrix was also defined by subtraction of gravity measurement on aligned axis. By subtraction, effects of fixed bias are removed and sensor output from gravity were doubled [9], so results were divided by 2 and can be measured in unit of local gravity. From online resources, local gravity at Seattle equals to 9.82978 m/s^2:

$$\begin{bmatrix} a_x^s & 0 & 0 \\ 0 & a_y^s & 0 \\ 0 & 0 & a_y^z \end{bmatrix} = \frac{1}{2}\begin{bmatrix} Acc_x^+ - Acc_x^- & 0 & 0 \\ 0 & Acc_y^+ - Acc_y^- & 0 \\ 0 & 0 & Acc_z^+ - Acc_z^- \end{bmatrix} \div g_{local} - I_{3\times3} \tag{62}$$

It can be solved that:$a_x^s = -0.00277, a_y^s = -0.00299, a_z^s = 0.00531$ (gravity)

Accelerometer misalignment were calculated based on non-gravity axes measurements due to cross coupling. For the same reason results were divided by 2 and measured in local gravity:

$$\begin{bmatrix} 0 & m_{xy}^a & m_{xz}a \\ m_{yx}^a & 0 & m_{yz}^a \\ m_{zx}^a & m_{zy}^a & 0 \end{bmatrix} = \frac{1}{2} \begin{bmatrix} 0 & Acc_y^+ - Acc_y^- & Acc_z^+ - Acc_z^- \\ Acc_x^+ - Acc_x^- & 0 & Acc_z^+ - Acc_z^- \\ Acc_x^+ - Acc_x^- & Acc_y^+ - Acc_y^- & 0 \end{bmatrix} \div g_{local} \tag{63}$$

$$m_{yx}^a = m_{xy}a, m_{zx}^a = m_{xz}a, m_{zy}^a = m_{yz}a,$$

Note that misalignment angle of sensor and casing are small and ignorable compared to misalignment when being installed on the car.

The gyroscope calibration could follow the same math model, but measurements should be performed on a fixed rate rotation table that the team did not possess. Instead, a simple calibration based on pivot angle [10] was performed. Procedures were described as below:

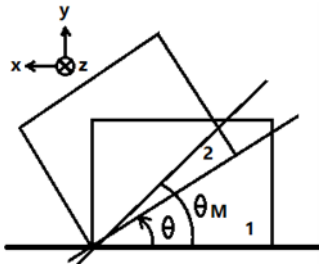

Figure 29: Gyroscope Pivot Angle and Measured Angle

- Chose a pivot point with horizontal surface and vertical edge around, calibrated the surrounding with level. External fastener was optional.
- Set initial and final position for IMU chassis alignment, preferably $\theta = 90$ degrees in between
- Placed IMU at initial position 5 minutes until thermal steady states, start logging. Recorded bias in angular rate from the average of the first 200 samples.
- Pivot slowly to final position in 3-5 seconds. External measurement on angle is optional.
- Hold at final position for 5 seconds, pivot IMU back to initial position at the same manner. Hold for another 5 seconds and complete logging.

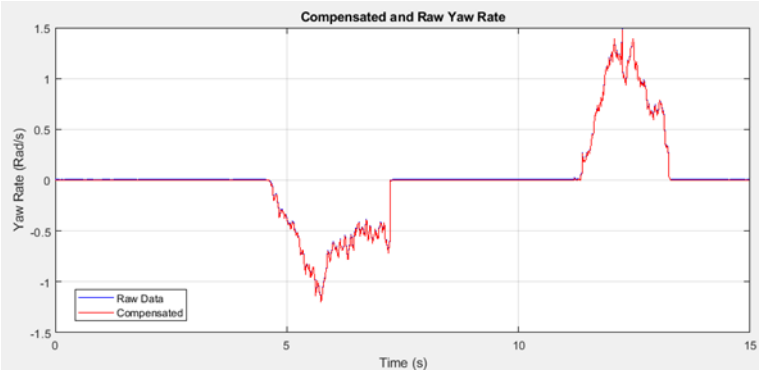

Figure 30: Yaw Rate of Pivot Test

Based on averaged yaw rate at first 200 sample, the offset bias error of gyroscope Z axis is: 0.003865 rad/s, comply to manual accuracy. By integrating uncompensated angular rate from 4 - 9 seconds, a rotation angle about 120 degrees were calculated. Scale-factor error were defined as:

$$average(\sum_{t=4}^{9} \frac{ActualAngle}{IntegrationResult}) = 0.7271 \tag{64}$$

VectorNav claimed to have built-in kalman filter that compensated for various readings, but its effectiveness had been unclear. As shown in the following graph, optional output of filtered angular rate was close to uncompensated rate within 15 seconds. With numerical integration, both angular rates resulted in angle prediction far from actual input. All rotational axis could be calibrated using method above.

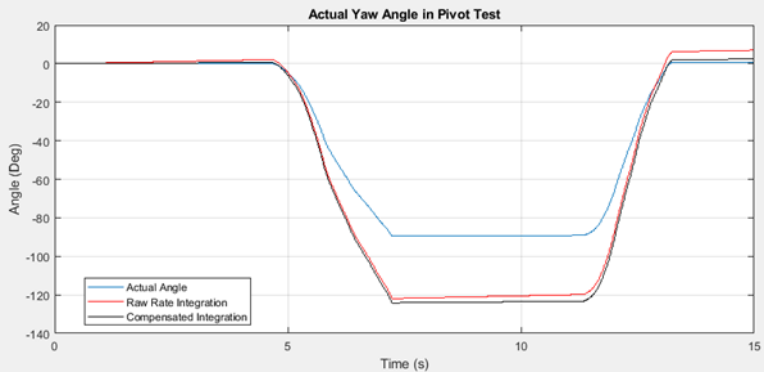

Figure 31: Scale-Factor Error of Gyroscope with Integration

All errors for accelerometer and gyroscope shall be removed using VectorNav control center. Calibrating on-vehicle IMU on a flat ground during competition shall be the first task after boot-up. The acceleration calibration was performed under 40 Hz and gyroscope under 80 Hz. When connected to serial CAN, frequency could be tuned as long as maximum baud rate does not exceed 115200.

5 Conclusion and Outlook

In this paper the author examined a PID based feedforward/feedback control to improve vehicle handling performance. A simulation of NMPC algorithm was performed as the skeleton when UWFM progressing toward L2 autonomous driving. Yet the full potential of vehicle had not been explored. Here are some of the topics that future members should investigate:

- Transient model of suspension should be investigated for riding analysis.
- System identification on roll dynamics should be performed to improve accuracy of normal force estimations. System identification of AC motor should be performed for FOC control.
- Understeer gradient should be measured by conducting constant radius experiments, on vehicle at open loop and with control. So that the handling limit can be quantitatively defined.
- Redundant sensors such as linear potentiometer on suspension and wireless torque control should be equipped for real-time feedback. A proper nonlinear kalman filter is needed on IMU.
- Vehicle models, and cost function for MPC should be well defined. Techniques such as pure-pursuit could be combined. Horizon and look-ahead distance should be optimized.
- When redesigning algorithm based on in-hub 4 motor powertrain, ground speed sensor may be required for accurate vehicle speed estimation.

6 Acknowledgement

The author would like to express sincere gratitude to Romain, Cedric, Antonio and Ryan from University of Washington Formula Motorsports. Special thanks to my committee for all the support to make this opportunity happen.

References

[1] Nguyen,H.(2019) *Traction Control and Torque Vectoring for the UWFM Electric Independent RWD Vehicle Körper*. University of Washington, 2019.

[2] Goran,v.,Bodan,S.(2016) *Model Predictive Control Based Torque Vectoring Algorithm for Electric Car with Independent Drives Körper*. 2016 24th Mediterranean Conference on Control and Automation (MED), 2016.

[3] Leonardo De Novellis, Aldo Sorniotti, Ptrick Gruber, Andrew Pennnycott.(2014) *Comparison of Feedback Control Techniques for Torque Vectoring Control of Fully Electric Vehicles Körper*. IEEE, 10.1109/TVT.2014.2305475 2014

[4] Kun Jiang, Adina Pavelescu, Alessandro Correa Victorino, Ali Charara. *Estimation of Vehicle's Vertical and Lateral Tire Forces Consider Road Angle and Road Irregularityörper*. 17th International IEEE Conference on Intelligent Transportation Systems, Oct 2014.

[5] Antunes,J., Antunes,A. Outeriro,P. Cardeira,C. Oliveira,P.(2019) *Testing of a Torque Vectoring Controller for a Formula Student Prototype, Robotics and Autonomous Systemsörper*. Robotics and Autonomous Systems, March 2019.

[6] Wheals, J. Deane, M. Drury, S. Griffith, G et al.(2006) *Design and Simulation of a Torque VectoringTM Rear Axleörper*. SAE Technical Paper 2006-01-0818,2006.

[7] Sawase,K., Ushiroda,Y.(2008) *Improvement of Vehicle Dynamics by Right-and-Left Torque Vectoring Systems in Various Drivetrainsörper*. Misubishi Motors Technical Review, 2008

[8] Tedaldi,D., Pretto,A., Menegatti,E.(2014) *A Robust and Easy to Implement Method for IMU Calibration Without External Equipmentörper*. 2014 IEEE International Conference on Robotics Autonation, May 31 2014.

[9] Ferguson,J.(2015). *Calibration of Deterministic IMU Errors örper*. Embry-Riddle Aeronautical University, 2015

[10] Looney,M.(2010) *A Simple Calibration for MEMS Gyroscopes örper*. Analog Device, EDN Europe July 2010.

[11] Qiu,J.W., Jiang,Yan., Xu,Wei.,et al.(2014) *Model Predictive Control for Self-driving Vehicles örper*. Beijing Institute of Technology Press, April 2014.

[12] Schildbach,G.(2020) *Vehicle Dynamics & Control YouTube Seriesörper*. University of Luebeck, May 2020.

[13] Schouwenaars,T., How,J., Feron,E.(2004) *Receding Horizon Path Planning with Implicit Safety Guaranteesörper*. American Control Conference, June 2004.

[14] Liniger,A., Domahidi,A., Morari,A.(2017) *Optimization Based Autonomous Racing of 1:43 Scale RC Carsörper*. Automatic Control Laboratory, ETH Zurich, 2017

[15] Liu,J., Jayakumar,P., Overhold,J.L., et al.(2013) *The Role of Model Fidelity in Model Predictive Control Based Hazard Avoidance in Unmanned Ground Vehicle Using LIDAR Sensors [C] örper*. Proceeding of ASME Dynamic Systems and Control Conference, 2013:1-10.

[16] Cong,Y., An,X., Chen,H., et.al.(2012) *Mobile Robotics Path Tracking Control Based on Receding Horizon örper*. Jilin University, 2012.

7 Appendix

Symbols	Variables	Units
δ	Steering Angle	deg(rad)
a,b	Front Rear wheelbase	m
L	Total wheelbase	m
R	Instantaneous radius	m
m	Vehicle mass	Kg
g	Gravitation Constant	$9.81 m/s^2$
a	Acceleration	m/s^2
I_z	Yaw moment of inertia	$Kg * m^2$
$C_{f,r}$	Cornering stiffness	N/deg(N/rad)
$v_{x,y}$	Long/Lat velocity	m/s
F	Force	N
ϕ	Yaw angle	Deg(rad)
M	Rotational momentum	Nm
α	Slip angle	Deg(rad)
λ	Slip ratio	ratio
$W_{f,r}$	Weight ratio	ratio
K	Understeer gradient	$deg * s^2/m$
ω	Wheel speed	RPM(rad/s)
R_w	Wheel radius	m
$T_{f,r}$	Trackwidth	m
$\mu_{\lambda,\alpha}$	Frictional coefficient	unitless
ρ_{air}	Air density	$Kg * m^3$
F_{tr}	Traction force	N
T_m	Motor torque	Nm
T_b	Damping torque	Nm
J_w	Wheel assembly inertia	$Kg * m^2$
ΔT	Torque difference	Nm

List of Figures